



## IoT protocols, architectures, and applications

Downloaded from: <https://research.chalmers.se>, 2025-12-05 01:48 UTC

Citation for the original published paper (version of record):

Buratti, C., Ström, E., Feltrin, L. et al (2021). IoT protocols, architectures, and applications. Inclusive Radio Communications for 5G and Beyond: 187-220.

<http://dx.doi.org/10.1016/B978-0-12-820581-5.00013-4>

N.B. When citing this work, cite the original published paper.



# Tunable spring balanced magnetic energy harvester for low frequencies and small displacements

Johan Bjurström<sup>a,d,\*</sup>, Fredrik Ohlsson<sup>a,b</sup>, Andreas Vikerfors<sup>c</sup>, Cristina Rusu<sup>a</sup>,  
Christer Johansson<sup>a</sup>

<sup>a</sup> RISE Research Institutes of Sweden AB, Gothenburg, Sweden

<sup>b</sup> Department of Mathematics and Mathematical Statistics, Umeå University, Umeå, Sweden

<sup>c</sup> ReVibe Energy AB, Gothenburg, Sweden

<sup>d</sup> Chalmers University of Technology, Gothenburg, Sweden

## ARTICLE INFO

### Keywords:

Vibration energy harvesting  
Electromagnetic induction  
Low frequency  
Small amplitude excitation  
Nonlinear dynamics  
Automotive safety

## ABSTRACT

In this paper we present a novel concept to efficiently harvest vibrational energy at low frequencies and very small displacement. We describe and evaluate an electromagnetic energy harvester which generates power from a magnetic circuit with motion induced variations of an air gap. External vibrations induce oscillations of the gap length around an equilibrium point, due to a linear spring counteracting the magnetic force. The relative position of the spring can be adjusted to optimize the harvester output for excitation amplitude and frequency. A simulation model is built in COMSOL and verified by comparison with lab measurements. The simulation model is used to determine the potential performance of the proposed concept under both harmonic and non-harmonic excitation. Under harmonic excitation, we achieve a simulated RMS load power of 26.5  $\mu\text{W}$  at 22 Hz and 0.028 g acceleration amplitude. From a set of comparable EH we achieve the highest theoretical power metric of 1712.2  $\mu\text{W}/\text{cm}^3/\text{g}^2$  while maintaining the largest relative bandwidth of 81.8%. Using measured non-harmonic vibration data, with a mean acceleration of 0.039 g, resulted in a mean power of 52  $\mu\text{W}$ . Moreover, the simplicity and robustness of our design makes it a competitive alternative for use in practical situations.

## 1. Introduction

Advances in fabrication techniques for semiconductors have enabled the development of very low power processor and wireless transmission systems. Research in energy harvesting (EH) aims to increase the number of small-scale applications which can be powered by ambient energy sources. The most evident benefit of self-sustained electronics is in cases where access is difficult or impossible and in cases where many units result in high maintenance costs or cumbersome power cabling. Areas that may benefit from energy harvesting are wireless sensor networks [1], such as the Internet-Of-Things [2,3] or smart agriculture [4–6], wearable electronics [7,8], autonomous vehicles [9–11] and predictive maintenance [12,13].

For automotive applications, specifically for autonomous vehicles, there is a need for increased safety for passengers and driving. This can be accomplished by integration of a large number of sensors. However, this is challenging to realize if batteries must be utilized (due to replacement need, inaccessible deployment, large quantities and

environmental impact). Alternatively, wired power distribution is needed, increasing weight/cost and complicating the installation due to limited space. The most promising solution is self-powered sensor systems. In this way, it reduces the weight and saves cost by reducing the amount of cables in the car without reducing the robustness of the system, allowing to increase the number of sensors in the car, reduce risks and increase safety.

One common source of ambient energy is movement, for example generated from moving/vibrating parts in devices or vehicles. This source of energy is one type utilized for our specific automotive application and is described here. The main requirements are low frequency (typically 20 Hz to 80 Hz), very low acceleration with a typical spectrum shown in Fig. 5, very small displacement (tens of microns range), non-harmonic and random displacement/excitation and small harvester size (below 20  $\text{cm}^3$ ). There are many transduction mechanisms which can be utilized to convert movement, i.e., mechanical energy, to electrical power. The general term for such a system is a vibrational energy harvester (VEH).

\* Corresponding author.

E-mail address: [johan.bjurstrom@ri.se](mailto:johan.bjurstrom@ri.se) (J. Bjurström).

<https://doi.org/10.1016/j.enconman.2022.115568>

Received 12 January 2022; Received in revised form 18 March 2022; Accepted 30 March 2022

Available online 7 April 2022

0196-8904/© 2022 The Author(s). Published by Elsevier Ltd. This is an open access article under the CC BY license (<http://creativecommons.org/licenses/by/4.0/>).

Peak transduction efficiency, resonance frequency, absolute and normalized bandwidth, applicable displacement range and size are key characteristics in any VEH. A multitude of techniques have been applied to improve these parameters when operating in the low frequency range. Non-resonant VEH have the benefit of intrinsically working in the ultra-low frequency (ULF) range and having a wide frequency operating range, the downside being that there is no enhancement of displacement amplitude (due to lack of resonance) [14,15]. Implementing non-linear behavior is a method which can be used to adjust the frequency range up or down as well as increase bandwidth (e.g., bi-stability [15,16], stoppers [17,18], spring non-linearity [19,20], non-linear damping [21] or non-linearities due to material properties [22–24]).

In this work, we will describe a novel concept for a VEH with beneficial characteristics for sensor applications in an automotive setting. Our concept builds on electromagnetic induction as its transduction mechanism and incorporates spring non-linearity for bandwidth widening and has the potential of dynamic frequency tuning.

An electromagnetic energy harvester (EMEH) relies on Faradays law, which relates the change in magnetic flux in a closed loop to electromotive force (EMF), as for example, by relative displacement between coil and magnet. The magnitude of this effect is relative to the local gradient of the magnetic field in the region of the coil, the rate at which it is displaced and the number of loops in the coil. The first two are key design factors to enhance when generating EMF. Local high gradients in the magnetic field can be achieved by e.g., magnet array configurations and/or by use of flux guiding components. The rate of displacement can be increased by e.g., frequency up-conversion as mentioned previously.

For the case of small displacements, in the range of tens of microns, and at low frequencies (<100 Hz), it becomes increasingly challenging to achieve sufficiently large magnetic field gradients and/or rate enhancement. We therefore propose to use the, to our knowledge, previously unexplored method of inducing flux variation in a coil by only altering the reluctance of a flux guiding circuit, while both coil and magnet remain static. We propose a solution where vibrational excitation induces variations in the air gap of a magnetic circuit, which is proportional to a change in reluctance.

Similarly with relative displacement of coil and magnet, the rate of displacement is also a key design factor. However, in our solution it is the displacement relative the total air gap distance which is most relevant and will be exploited in our VEH design. To achieve a significant coupling between EMEH movement and the time differential of magnetic flux in the air gap, as well as through the coil, the total air gap distance should be close to the amplitude of the air gap displacement. A large magnetic remanence from the magnetic field source is also a necessity to achieve large flux variation. For displacements in the range of tens of microns, these requirements give rise to a large force, acting to close the air gap. Our design therefore incorporates a low-profile spring to counteract the attractive force within the airgap. The stiffness of the spring is chosen to result in a small equilibrium distance of the air gap, around which external vibrations induce perturbations. We will show that the relation between spring force and magnetic force determines the resonance frequency of the system, as well as the energy which can be harvested from vibrations. With this in mind, we also explore the possibility of frequency-tuning by adjusting the position of the spring base relative the air gap. We will also show that the coupled magnetic and spring force results in a non-linear system with the effect of increased bandwidth.

To our knowledge, this method of electromagnetic energy harvesting, with the potential of frequency tuning by air gap variation, has not been previously explored. This method has the advantage of allowing not only frequency tuning, but also excitation amplitude tuning, i.e., to allow harvesting from smaller excitation force we can reduce the equilibrium distance of the air gap and vice versa. The design complexity of the magnetic source is also reduced as we do not need to design for large magnetic field gradients. The method also allows for a low-profile design (i.e., size in the main direction of vibration) as the change in reluctance,

and thus harvesting performance, benefits from a large area rather than height.

Our method is well suited for applications in automotive safety as it can be tuned to the typical vibration environment of low frequency and small displacement. The possibility of frequency tuning together with the wideband operation of our EH is also beneficial for the typically stochastic in-car vibrations. Another benefit is the potentially low-profile design which simplifies integration with existing structures.

Section 2.1 of this paper will describe the prototype design in detail as well as the operational behavior. A more detailed description of the novel concept, together with the simulation FEM model, will be given in Section 2.2. Section 2.3 will describe the measurement setup and test procedure. Measurement and simulations results are given in Section 3 together with a discussion of the results and a comparison with the state of the art. A brief discussion on what future work may entail is also given.

## 2. Experimental methods

### 2.1. Magnetic energy harvester design

The concept of the spring balanced magnetic circuit is implemented in an axisymmetric design. Fig. 1 shows the constituents of the proposed EMEH. A cylindrical, ring shaped, magnet generates the magnetic flux. Two separate soft magnetic parts guide a portion of the flux into a coil. The two soft magnetic parts (henceforth called “the core”) can move relative to each other, tethered by a spring. The spring may be positioned on the outside of the EMEH (easier to optimize but increases EMEH size) or in the air gap (most efficient use of space but increases design complexity). The amount of flux being guided into the coil depends primarily on the magnetic reluctance of the air gap relative to the reluctance of the region outside the EMEH. In this case, the air gap reluctance varies due to a varying air gap size. As the flux focuses along the shortest path around the magnetic circuit, regions far away from the magnet are best utilized for the proof mass.

### 2.2. Concept theory and FEM model

Figure 2a outlines the basic principle of the proposed concept. It shows the two counteracting forces, the repulsive spring force (red) working to increase the air gap and the attractive magnetic force (blue) working to close the air gap. As the spring is compressed at decreasing air gap it follows the linear relationship  $F = k(\beta - x)$ , where  $x$  is the air gap distance,  $k$  is the spring constant and  $\beta$  is the offset of the spring base relative the air gap closed state (i.e.  $x = 0$ ), henceforth referred to as “spring offset”. The spring offset can be seen as a tuning parameter, which in Fig. 2a is given an arbitrary value. The magnetic force in Fig. 2a is extracted numerically from the FEM simulation tool COMSOL using the same model geometry as in Fig. 1 and idealized material parameters. To simplify the description of the basic principle, the magnetic hysteresis is here assumed negligible when generating the blue curve for Fig. 2a. In all following simulations, the effect of magnetic hysteresis is included. It is assumed that the basic principle described here still holds if a sufficiently small magnetic hysteresis is achieved.

There are two points where the total force sums to zero. At the stable point (A) there is a net restoring force in each direction, equal to the difference between the blue and red curve. At the unstable point (B), the air gap will either be reset to the stable position or seal shut. In practice, the unstable position is always reached with some remaining momentum. It will thus always end up in the shut state, unless a stopper is implemented, or the counteracting force is modulated (by e.g. spring non-linearity or a secondary linear spring). Fig. 2b shows the corresponding potential energy of the magnet-spring system, with a potential well at point A.

The non-linearity of this EMEH stems from the non-linear magnetic force (Fig. 2a), resulting in a non-linear restoring force. The coupled

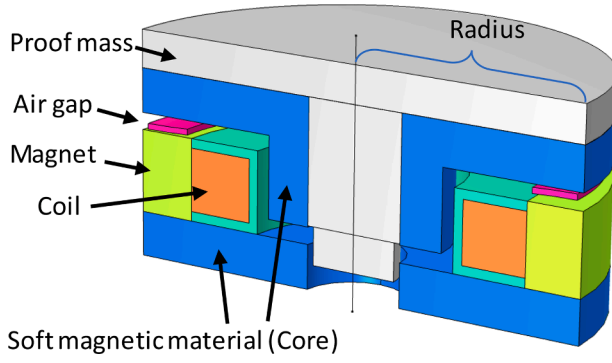


Fig. 1. Electromagnetic energy harvester concept design with ideal spring placement. Schematic of geometry and constituents.

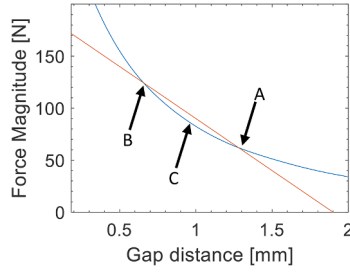


Fig. 2a. Magnitude of opposing forces. Blue: Magnet force. Red: Spring force. A: Stable equilibrium. B: Unstable equilibrium. C: Local maxima in restoring force. (For interpretation of the references to colour in this figure legend, the reader is referred to the web version of this article.)

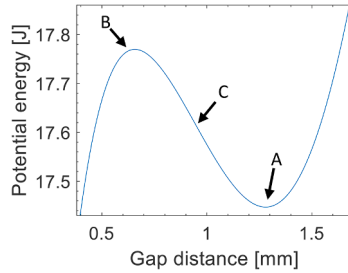
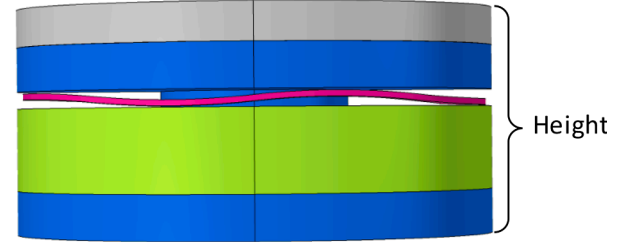


Fig. 2b. Potential energy of magnet-spring system. A: Stable equilibrium. B: Unstable equilibrium. C: Local maxima in restoring force.

non-linear magnetic and linear spring force, effectively results in a non-linear spring system, with a potential energy diagram according to Fig. 2b. Decreasing the offset of the spring position relative the magnetic circuit leads to a downward shift of the linear spring force (red) in Fig. 2a. This results in a reduced potential well at point A, both in width and depth. In this case, the energy required to reduce the air gap decreases as well as the range of movement before the unstable point (B) is reached. The inflection point in Fig. 2b (C) corresponds to a local maxima in restoring force, i.e. between point B and C the force required to decrease the gap distance also decreases with gap distance. At this point (C) the non-linearity between the external acceleration and the proof mass displacement will significantly increase.

The concept has been implemented and numerically evaluated in the FEM simulation tool COMSOL. A 2D axisymmetric model is used, with a cylindrical geometry (see Fig. 1). The radius of the EMEH in the COMSOL model is 18.5 mm and the height is approx. 18 mm (including proof mass displacement). COMSOL modules “Magnetic Fields” and “Electrical Circuit” are used to calculate the magnetic flux, resulting magnetic forces and the EMEH power output over time. An ordinary differential equation (eq. (1)) is used in COMSOL to model the change in air gap



distance (or equivalently, proof mass displacement) resulting from an external force ( $F_{Ext}$ ), linear spring force ( $k(\beta - x)$ ) and magnetic force ( $F_{mag}$ ).

$$M\ddot{x} + F_{mag} + C\dot{x} - k(\beta - x) + F_{Ext} = 0 \quad (1)$$

The velocity and position of the proof mass are denoted as  $\dot{x}$  and  $x$ . Mass, mechanical damping and spring coefficient are respectively denoted as  $M$ ,  $C$  and  $k$ .  $F_{mag}$  is numerically determined by the Magnetic Fields module within COMSOL and includes the effect of electrical damping from the coil and damping from eddy currents in the core. As the spring is assumed to act only in the linear regime, all non-linear characteristics of the EMEH are contained in  $F_{mag}$ . The external force is denoted by  $F_{Ext}$ . Both a prescribed harmonic force and a stochastic external acceleration have been used ( $F_{Ext} = M\ddot{y}$ ). The corresponding free body diagram is shown in Fig. 3.

The Electrical Circuit module in COMSOL uses a simple resistive load, matched to the resistance of the coil. Rectification and power storage are not included in the model. The electrical module includes both the resistance and inductance of the coil.

The COMSOL model uses event handling to account for collision with a stopper. For simplicity, the collisions are assumed to be completely inelastic. For a stiff stopper this assumption is likely realistic. However, an elastic stopper (or spring) would be preferable in order to preserve and harvest more energy.

Magnetic hysteresis is included in the model even though it is neglected in the above concept description. This is a necessary inclusion to be able to compare the COMSOL model with a non-ideal prototype. The flux guiding core therefore uses a 5-parameter Jiles-Atherton (J-A) model [25,26] for magnetic flux calculations, which includes a hysteretic effect when magnetizing and demagnetizing the core. The J-A model accounts for an impedance to magnetic domain wall movement and rotations, which in turn leads to a hysteretic effect. The considered impedance arises from “pinning sites” in the magnetic material, i.e.

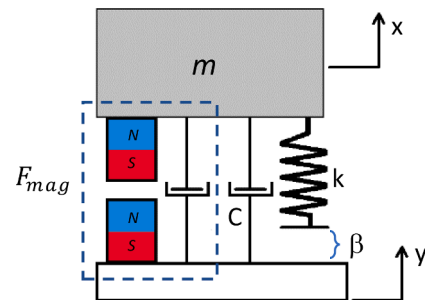


Fig. 3. Free body diagram.  $F_{mag}$  represents both magnetic force and damping from eddy currents and energy harvesting.  $C$  is the mechanical damping coefficient and  $k$  is the spring constant.  $\beta$  is the spring offset, i.e. the offset of the spring base relative the air gap closed state.

areas of decreased permeability for the magnetic domain walls due to imperfections in the magnetic material [25,26]. The J-A parameters are defined in Table 2 below.

A number of in situ measured vibrational acceleration datasets, acquired in automotive settings, have been available during simulation [27]. We import a set of measured data to COMSOL and use it to determine  $F_{Ext}$  in eq (1). Fig. 4 shows the raw data from this dataset, which has been used in simulations for this work. The corresponding acceleration spectral density plot in Fig. 5 shows a concentration of kinetic energy around 40 Hz.

### 2.3. Prototype and measurement setup

A prototype was built using commercially available magnet, spring and core material based on the concept shown in Fig. 1. The design was altered to fit with these commercial components. Supporting structures were 3D printed in polyamide. The proof mass and core components were CNC machined from brass and iron (AISI 1018 low carbon steel, with Saturation approx. 2.08 T, coercivity approx. 770 A/m and retentivity approx. 1.13 T [28]) respectively. The dimensions of the core components are the same as in the simulation model. A stainless-steel wave spring from Smalley is used to counteract the magnetic gap force. The spring constant is 100 N/mm  $\pm$  10%. The magnet is of neodymium with an energy grade of N36 (remanence is approx. 1.2 T). The coil is wound with 0.1 mm copper wire (1680 windings). Once assembled, the prototype consists of three parts (see Fig. 6). The proof-mass, one flux guiding component and spring are glued together (first part). Magnet, coil, primary structural support and the offset plate are glued together (second part) and held static relative to the secondary structural support (third part). The vertical position of the offset plate determines the spring offset  $\beta$  and thus the working point of the spring, i. e. the spring force at a given air gap distance, and is used to tune the EMEH to higher efficiency. Thin shims of known thickness (0.1 mm to 1 mm) are placed around the axis of the offset plate passing through part 3. The number of shims and their thickness is used to adjust the vertical position of the offset plate. The offset plate has threads making it possible to lock it in place. Excluding the additional parts compared to Fig. 1 (structural supports and offset plate) the large proof mass adds 1.3 mm of height (total height is then 19.3 mm) and extends the radius to 32 mm.

In the measurement setup, a shaker excites the EMEH by applying a harmonically oscillating force directly on the proof mass to simulate vibrations subjected to the EMEH (Fig. 7a). The shaker is positioned to apply a small constant force bias to ensure contact with the EMEH throughout the displacement range. A calibrated thin film FlexiForce sensor (standard model A201, Tekscan) is placed in the interface between shaker and EMEH. The net force in the interface is the difference between applied force (from shaker) and mass times acceleration of the proof mass. The proof-mass is in this configuration facing down. The driving current to the shaker is adjusted until a force amplitude of roughly 0.3 N measured. The EMEH load voltage is continuously sampled at 51.6 kb/s via a digital-to-analog converter (DAC) using

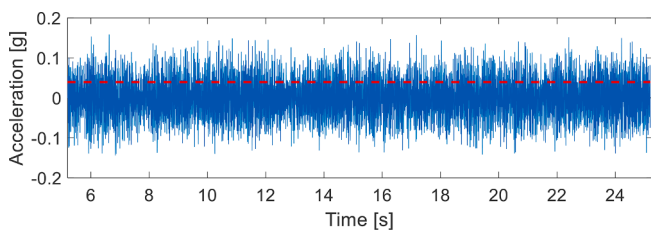


Fig. 4. In situ measured vibrational acceleration data from automotive source. Dotted red line shows the mean of the acceleration magnitude at 0.039 g. (For interpretation of the references to colour in this figure legend, the reader is referred to the web version of this article.)

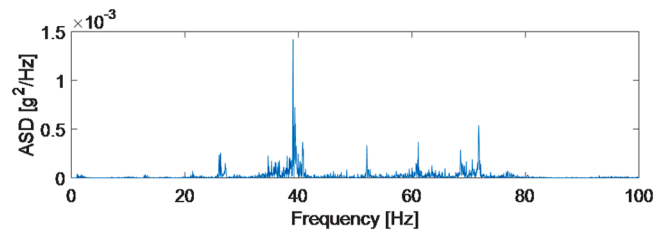


Fig. 5. Acceleration spectral density of measured acceleration.

MATLAB software. The load voltage is measured over a 300  $\Omega$  resistor (closely matching the measured resistance of the coil used in the lab prototype).

The frequency response of the EMEH was measured by sweeping the shaker frequency from 40 Hz to 130 Hz. During the frequency sweep the DAC continuously samples the load voltage with a sampling time of 1 s. The frequency of the signal driving the shaker is not known in the DAC sampling software and must be extrapolated from measured data. MATLAB is used to extract the load voltage RMS value and frequency for each time-resolved data set. The frequency corresponding to each data set is determined from the frequency spectra of the data set. Built in MATLAB functions for the Fast Fourier Transform (FFT) are used to generate the spectra. The frequency of the measured data set is then taken to be the largest component in the frequency spectrum for the data set.

A separate test-rig was built to measure the gap force for varying gap distance (Fig. 7b). From the diagram in Fig. 6, only the magnet and core components were used. The spring is not included and thus only the force resulting from magnetic flux in the air gap is measured. Magnet and one core component were mounted statically. The second core component was mounted on a rod passing through the center of the magnet and resting on a vertically adjustable base. The force was measured by placing a FlexiForce<sup>TM</sup> sensor between rod and base. A second rod was used to limit horizontal movement with minimal friction. Shifts in the vertical position of the rod and core component were measured using a digital dial indicator (Mitutoyo 543–782).

### 3. Results and discussion

The purpose of the results within this work are to validate the COMSOL simulation model and to determine the potential performance of the EMEH system under both harmonic excitation and real vibration conditions.

#### 3.1. Validation of simulation model

Validation of the COMSOL simulation model is achieved by comparing results from prototype measurements and equivalent simulations. The first characteristic to evaluate is the effect of magnetic hysteresis in the prototype EMEH. As we are only interested in the resulting hysteresis in air-gap force vs air-gap distance, we do not measure the B-field in the core as a result of magnetization (typical B vs H curve), instead we use the measurement setup described earlier. The gap force is proportional to the square of the magnetic flux through the gap (and in the same manner proportional to the B-field) [29]. The flux is in turn proportional to the gap reluctance (or indirectly the gap distance). Fig. 8 shows the gap force vs air-gap distance, both measured (blue) and simulated in COMSOL (red). When measuring the force, the gap distance was varied approx. 4.5 mm. The gap distance was swept twice between the endpoints which is the reason for the overlapping data (blue). In both simulated and measure data, the part of the curve with larger force corresponds to increasing the gap distance. To quantify the difference in gap force hysteresis, we compare the relative difference (arbitrarily chosen at a gap distance of 1 mm) between the force during magnetization and demagnetization of the core. The simulated data



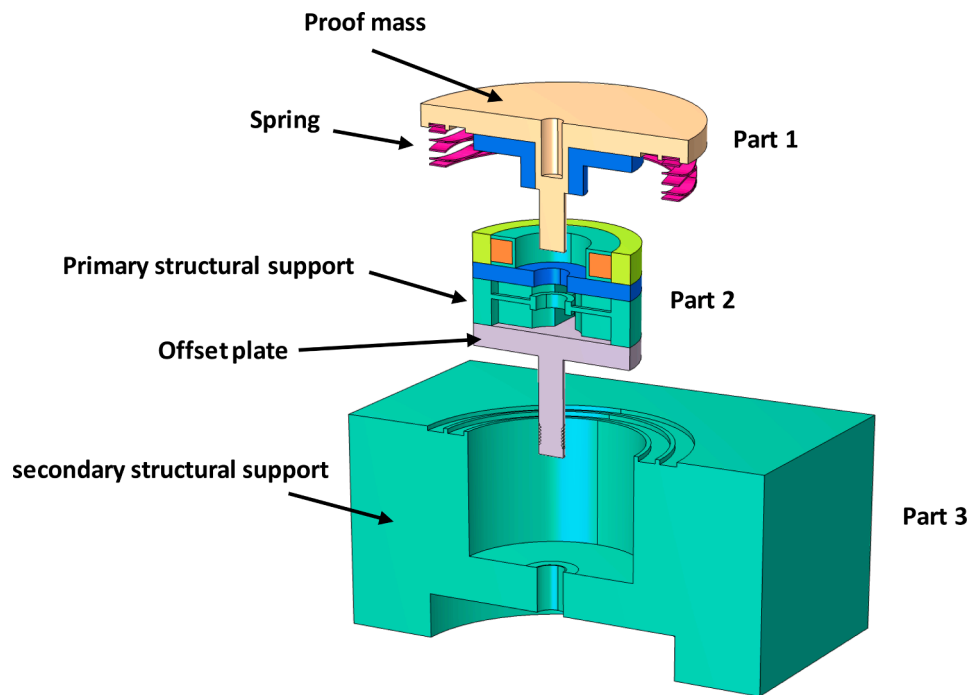


**Fig. 6.** Exploded diagram of prototype. Top: Part 1 consisting of proof mass, spring and core component. Middle: Part 2 consisting of magnet, coil, core component, offset plate and support structure. Bottom: Part 3 is used as support structure.

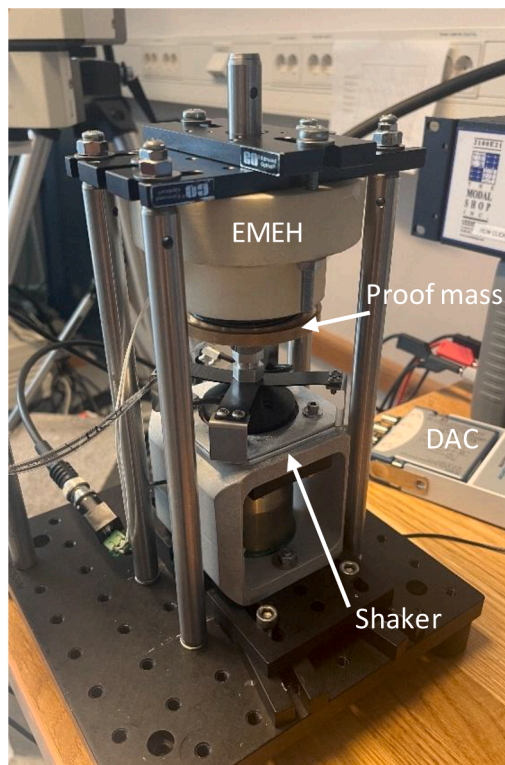


**Fig. 7a.** Test setup for applying harmonic excitation force on EMEH.

shows a relative difference of 8% whereas the measured data shows a difference of 16.5%. In absolute terms the difference in force is approx. 7.2 N larger for the measured curve. As the excitation amplitude used in the lab setup is only 0.3 N, the effect of this larger hysteresis on the EMEH output is likely significant.

We could not find the JA parameters for AISI 1018 low carbon steel

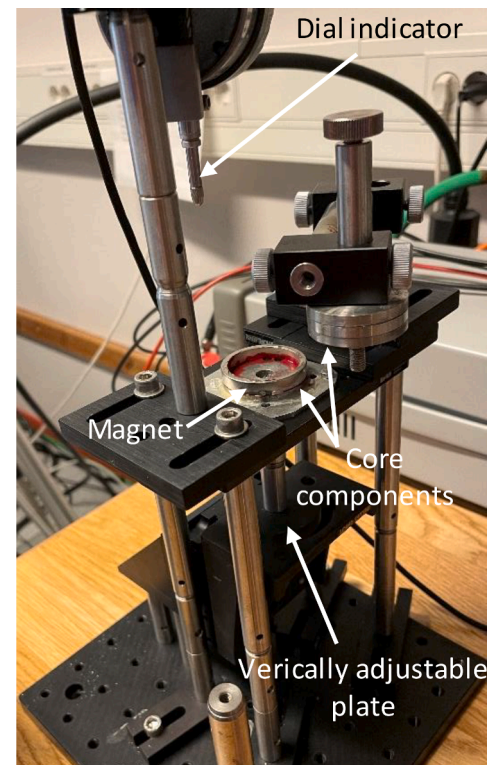


**Fig. 7b.** Setup to measure gap force at varying gap distance. Only the force due to magnetic flux in the airgap is measured, i.e. no spring.

described in literature. The JA parameters used in our simulations are therefore based on those derived by Jiles et. al. [26], valid for Fe-C 0.06 wt% (other constituents of the alloy were not mentioned in [26]). Other components such as manganese may also be of importance. E.g., previous work by Jiles et. al. [25], using 1% manganese steel showed a

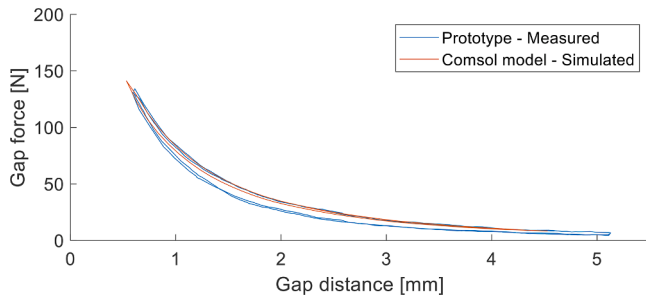


**Fig. 8.** Gap force resulting from magnetic flux in the air gap (i.e., spring is not included). Measured (blue) and simulated (red) gap force. Top part of hysteresis curve corresponds to increasing the gap distance. (For interpretation of the references to colour in this figure legend, the reader is referred to the web version of this article.)

roughly 3x larger value of “a” and 3x smaller value of “k”. AISI 1018 low carbon steel has a carbon content of 0.14%–0.2% and manganese content of 0.6%–0.9%. This difference in alloy composition may have a significant effect on the JA parameter values. We chose to use values of “ $\alpha$ ”, “ $M_s$ ” and “a” that closely match those given by [26], while “c” is set to a factor of 10 smaller. “k” was varied in order find a value giving a closer match between measured and simulated gap force hysteresis. Between a “k” value of 2000 A/m and 3000 A/m, we did not see a significant increase in gap force hysteresis. This set of parameter values (see Table 3) still does not manage to recreate the same degree of hysteresis as in the measured data. It is possible that the range of our parameter space was insufficient to find a better match. The geometry and alignment of the magnetic core components determine the proportionality between magnetization and gap force. It is unlikely that small geometric discrepancies are the reason for the difference in gap

force hysteresis between simulated and measured data.

Frequency sweeps of a sinusoidal excitation force were performed both in simulation and using the measurement setup. A set of power spectra were acquired with varying spring offset  $\beta$  (in the case of the measurement setup, the position of the offset plate, see Fig. 6, was varied and measured). The hysteresis is the same as shown in Fig. 8. Fig. 9 shows the set of simulated power and the measured power. Due to the limited precision of the spring offset in the measurement prototype (0.1 mm) we could not match exactly the spring offset used in simulation.

The applied force amplitude used in the simulations is 0.3 N and is measured to be approximately the same in the lab. The minimum spring offset used in the lab measurements is 1.95 mm. At 1.85 mm the EH would get stuck in a closed state (as described in Section 2.2). Both measured and simulated data follow the same pattern for increasing spring offset, i.e. an increase in resonance frequency and a decrease in bandwidth. Simulations were performed in the time domain for each excitation frequency, after which the RMS power was derived for each frequency. To achieve reasonable simulation times for each power spectra the time step could not be set too small. For certain sets of JA parameter values this leads to significant computational errors. Although these computational errors hamper the comparison between peak power (see Fig. 9) results indicate a larger simulated peak power compared to what was measured. The bandwidth of the measured spectra is overall larger than the simulated results. The difference in peak power and bandwidth could, in part, be due to the larger hysteresis in the prototype (Fig. 8).

The increase in peak power at increasing spring offset is most likely due to the EMEH configuration being increasingly efficient at the specific excitation force amplitude of 0.3 N. For a given excitation force there is likely an optimum spring offset and vice versa.

The shaker will experience some force feedback from the EMEH. How the shaker responds to this has not been accounted for in the

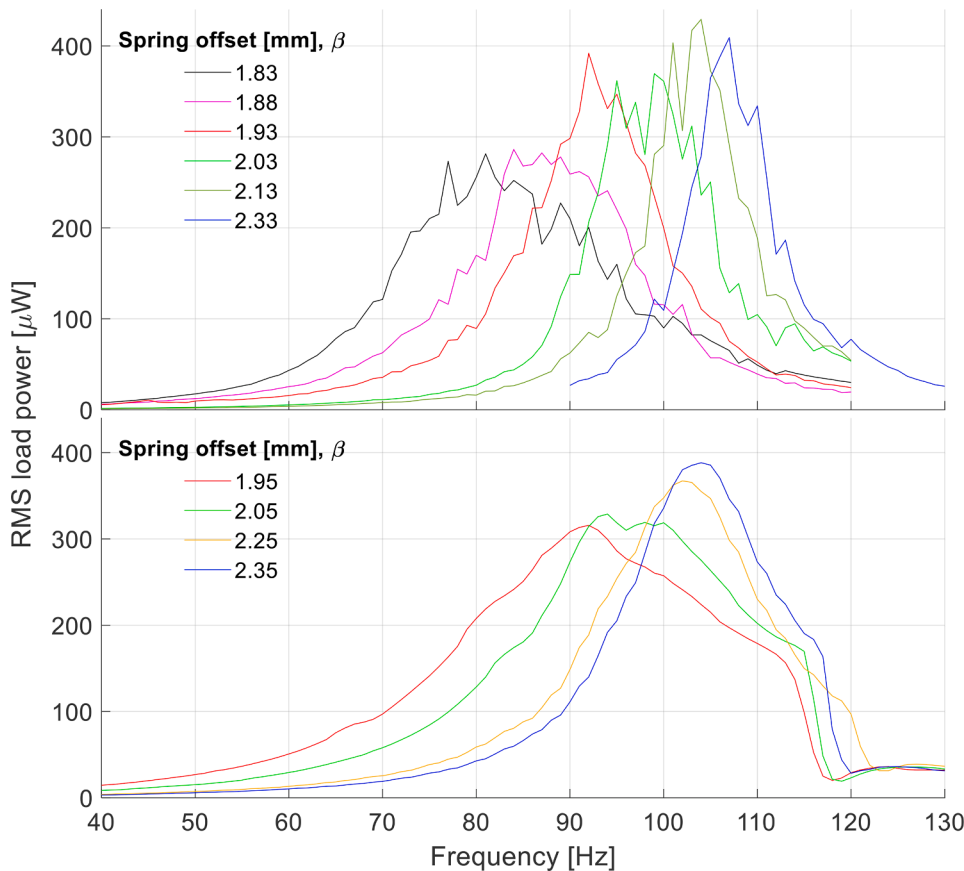


**Fig. 9.** Simulated (Top) and measured (bottom) RMS load power. Red, Green and Blue are used to indicate data sets using similar spring offset. The spring offset used in measurements is set to match the simulation model parameters as closely as possible. The full set of model parameters values are found in Table 1 and Table 3. In both simulation and lab prototype, a further decrease in spring offset put the system in a permanently closed state. (For interpretation of the references to colour in this figure legend, the reader is referred to the web version of this article.)

measured dataset above.

The relationship between spring offset and resonance frequency of the EMEH (with a resistive load only) has not been rigorously established in this work. The simulated results in Fig. 9 indicate that, when using parameter values as in Table 1 and Table 3, a spring offset position precision of roughly 50  $\mu\text{m}$  is required for a frequency tuning precision of 5 Hz, in the range  $1.83 \text{ mm} \leq \beta \leq 1.93 \text{ mm}$ . The sensitivity is nonlinear with respect to spring offset and decreases with increasing spring offset, i.e. the increase in resonance frequency, per  $\mu\text{m}$  shift in spring offset, decreases at increasing spring offset. Reducing the spring offset places the linear spring force curve closer to the knee of the nonlinear magnetic force curve (see Figure 2). The difference between the curves, close to the working point, is in this case also reduced. It is our assumption that this behavior is what defines the change in resonance frequency when adjusting the spring offset. The lowest resonance frequency would then correspond to the working point where the slopes are most similar. The lower frequency limit is at the point when the spring force is always smaller than, or equal to, the magnet force. The upper frequency limit is when the magnet force is approximately linear, and the difference between the curves becomes independent of spring offset.

To determine if the decreased measured power output, compared to simulations, (see Fig. 9) could be due to the larger hysteresis (Fig. 8), simulations were performed at decreasing degree of hysteresis. The hysteretic effect was in this case modulated by varying only the  $k$ -parameter in the J-A model. Table 4 quantifies the difference in hysteresis by comparing the force during magnetization and demagnetization (at a gap distance of 1 mm). The remaining parameters were chosen to result in a relatively large hysteresis.

Figure 10 shows the resulting simulated power spectrum for each value of  $k$ . As previously, an excitation force amplitude of 0.3 N is used. Although a magnetic remanence of 1.4 T was used for this set, the comparison with previous simulations, with regards to peak shifts, still holds. The initial decrease in power is assumed to be the same effect as seen in Fig. 9, which showed a decreased peak power at decreasing offset of spring force relative to the magnetic force. The increased peak power when decreasing  $k$  is primarily from the reduced hysteretic effect (also supported by Fig. 12). For each simulated data set, the spring parameters are unaltered, and as the magnetic force curve varies with varying  $k$ , there is thus a shift in resonance frequency.

### 3.2. Performance evaluation

To determine the potential capabilities of the EMEH described here in, we use the COMSOL simulation model with material and spring parameters adjusted to best suit the intended use. We assume a minimized hysteresis is optimal and achieve this by using J.A. parameter values modeled by Thomas et. al. [30] (based on a laminated iron core). We have also assumed negligible damping from eddy currents. Fig. 11 shows the resulting hysteresis curve (red) together with the same measured hysteresis (blue) as in Fig. 8. The difference in force at 1 mm, for the

**Table 1**

COMSOL parameter settings. The mechanical damping is set to 2% of critical damping. The load resistance is set to match the coil resistance as derived by COMSOL. The remaining parameters match those of the lab prototype EMEH developed within this work.

Model parameters	Value
Proof mass weight	180 g
Coil wire	SWG 42
Number of coil windings	1680
Perm. Magnet remanence	1.2 T
Load	271.5 $\Omega$
Mechanical damping, C	5.37 kg/s
Spring constant, k	100 N/mm
Core magnetization	JA-model

**Table 2**

Definition of Jiles-Atherton parameters.

J-A parameter	Representation
$\alpha$ [Unitless]	Interdomain coupling
$a$ [A/m]	Domain walls density
$M_s$ [A/m]	Saturation magnetization
$k$ [A/m]	Average energy required to overcome pinning site
$c$ [Unitless]	Magnetization reversibility

**Table 3**

J-A parameters used to match characteristics of prototype core material as closely as possible.

J-A parameters	
$\alpha$	0.0016
$k$	2000 [A/m]
$c$	0.02
$M_s$	1.7e6 [A/m]
$a$	1500 [A/m]

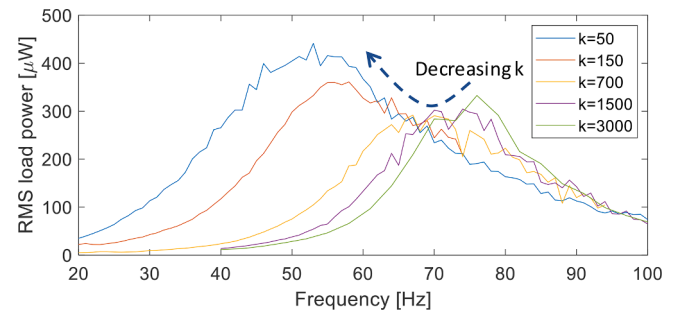
**Table 4**

Left:  $k$  values used in sweep and resulting hysteresis quantification (defined at a gap-distance of 1 mm). Right: J-A parameters used during  $k$ -sweep.

Parameter sweep		
$k$ -value [A/m]	Relative diff [%]	Absolute difference [N]
50	0.24	0.25
700	2.86	2.96
1500	5.25	5.35
3000	8.61	8.57

J-A parameters	
$\alpha$	0.0016
$k$	Param. sweep
$c$	0.02
$M_s$	1.7e6 [A/m]
$a$	1500 [A/m]



**Fig. 10.** EMEH RMS load power spectrum for different values of the J-A parameter  $k$ . The remaining J-A parameter values are constant (see Table 4: Right). The models use a spring constant of 100 N/mm and spring offset of 2.11 mm. The remanence of the magnet in each of these simulations is 1.4 T.

simulated curve, is in this case approx. 0.1% or 80mN.

#### 3.2.1. Excitation using harmonically applied force

We compare the frequency response of this low hysteresis model with the measured frequency response of the lab prototype (compare Fig. 9 with Fig. 12). The spring constant is here set to 50 N/mm and the approximate minimum spring offset, before the system gets stuck in a closed state, is 2.533 mm. As previously, increasing the spring offset increases peak power and increases the resonance frequency. Compared to the model used in Fig. 9 the resonance shift per mm increase in spring offset is significantly larger for the low hysteresis model. As previously



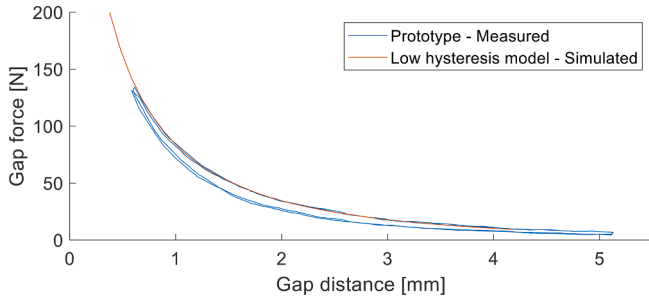


**Fig. 11.** Measured gap force (blue) and simulated gap force (red) using Jiles-Atherton parameters specified in Table 5. (For interpretation of the references to colour in this figure legend, the reader is referred to the web version of this article.)

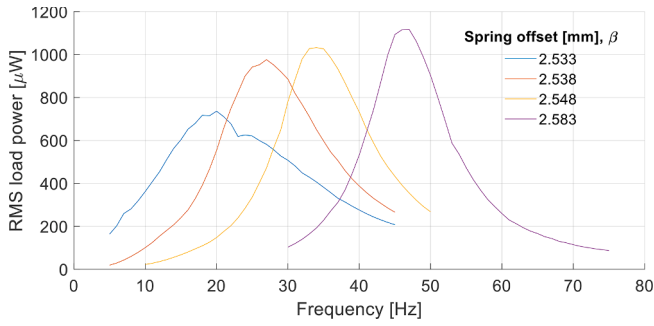


**Fig. 12.** Simulated load power using the low hysteresis model. The simulation model uses the low hysteresis J-A parameters of Table 5, a spring constant of 50 N/mm and spring offset of 2.533 mm.

the sensitivity is non-linear with respect to spring offset and is between 0.14 Hz/ $\mu\text{m}$  and 0.7 Hz/ $\mu\text{m}$  in the range 2.533 mm  $\leq \beta \leq$  2.548 mm. The same excitation force amplitude as for previous simulations is used (0.3 N). The results show that choosing materials with small hysteresis and optimizing the spring offset can result in higher power output at lower frequency. A similar result may be achievable by adjusting the design geometry to reduce the magnetization (resulting in a smaller hysteresis loop) while maintaining air gap flux.

As stated earlier we expect the nonlinear behavior of our EMEH to increase with increasing excitation force (see Section 2.2). An expected effect of this is an increase in bandwidth. The bandwidth broadening was verified by simulating the frequency response at increasing excitation force. Fig. 13 shows the normalized (by maxima) frequency spectrum at three different excitation forces. A 33% increase in absolute bandwidth, defined by the full width half maximum (FWHM), when increasing the force from 0.1 N to 0.3 N, was seen in simulation. The FWHM at 0.3 N force is 24 Hz and the resonance frequency is 20 Hz,

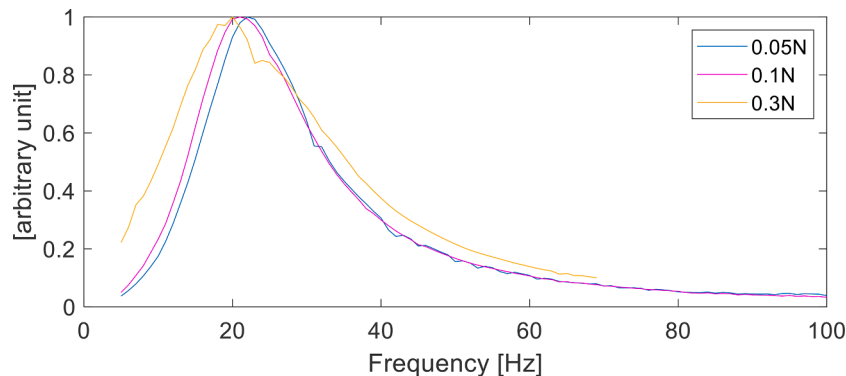


**Fig. 13.** Effect of excitation force on frequency response bandwidth. The curve for 0.3 N is the normalized result of the simulated data in Fig. 12.

leading to a relative bandwidth of 120% (absolute bandwidth/resonance frequency).

### 3.2.2. Excitation using in situ measured vibrations

Next we adjust the spring offset to give a power spectrum peak close to 40 Hz (see Fig. 14) as this is the frequency around which the vibration data from Fig. 4 shows most kinetic energy. The same material properties as in Fig. 12 are used. With a harmonic force excitation of amplitude 70mN (corresponding to an excitation acceleration of approx. 0.039 g), the peak power is 57.5  $\mu\text{W}$  and the FWHM is 14 Hz. The relative bandwidth is then 36%. The simulated load power using vibration data as excitation is shown in Fig. 15. The generated mean power is 52  $\mu\text{W}$  (RMS power is not used as the signal is non-harmonic).

### 3.3. Comparison to state of the art

Making a fair comparison with other energy harvesters is a relatively complex task, with a number of relevant parameters [31]. In the field of low frequency energy harvesters, the resonance frequency could be seen as a performance metric, with lower frequency being better. However, with our automotive application in mind the frequency range of most interest is between 20 Hz and 80 Hz. Thus, we do not find it relevant to benchmark our results against other EMEH with resonance frequencies far below this interval. In Table 6. We compare the performance of EH with an electromagnetic component and resonance frequency close to 22 Hz. The results presented for our work are based on simulations using the same model as described earlier, with minimized hysteresis and negligible eddy current damping, and using an excitation force amplitude of 50mN.

We have chosen to utilize the relatively simple performance metric  $P_{\text{avg}}/(\text{volume} \times \text{acceleration}^2)$  [32–34] when comparing EH. Volume, resonance frequency, power output and acceleration amplitude are included as supporting information and should not be directly compared. We include the relative bandwidth, which accounts for the fact that a spectrum with low center frequency has an intrinsically limited maximum bandwidth and can be viewed as a measure of performance. Finally, we include the size of the harvester along the main axis of movement ( $L_z$ ), as the power output typically has a larger

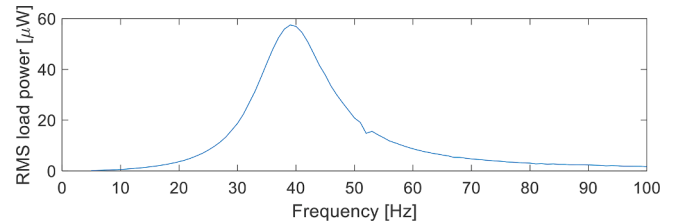


**Fig. 14.** Frequency response using parameterization tuned to 40 Hz.

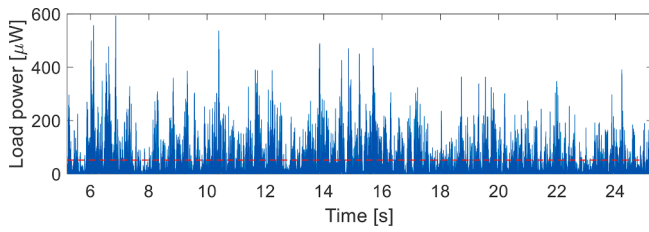


Fig. 15. Simulated load power using measured vibration data as input. Dotted red line shows the mean power of 52μW.

Table 5

Jiles-Atherton parameter values corresponding to a laminated iron core [30].

J-A parameters	
$\alpha$	7.9520e-5
$k$	59.3 [A/m]
$c$	0.5476
$M_s$	1.47e6 [A/m]
$a$	40 [A/m]

dependance on this size parameter compared to harvester size along the perpendicular dimensions [19].  $L_z$  refers to the total size including proof mass displacement.

Rigorous optimization has not been done in this work and only spring offset has been qualitatively analyzed for an optimal value. As stated earlier the model must implement either a stopper or additional spring. In our simulations we have only used a completely inelastic stopper. Both stopper position and elasticity (or in the case of an additional spring, the spring constant) are significant parameters for optimization. There is also the possibility of implementing a non-linear force to counteract the gap force (by non-linear spring or additional magnet), which should enable resonance at lower frequencies. The effect on performance of our EH concept when scaling the size, both isotropically and anisotropically, has not been investigated.

The simple and compact design of our EH should enable cost effective fabrication and be beneficial for robustness. The required precision of tuning (with regards to the spring offset) needs to be addressed as it either requires precise manufacturing or a finetuning mechanism with an effective travel range (in  $\mu\text{m}$ ) of approx. 10 times the desired frequency tuning. The possibility of active tuning, by e.g. a piezoelectric element, has not been explored within this work. The choice of material may become critical as size and environment requirements may limit choices of very low hysteresis materials.

Table 6

Performance metrics of a set of EH with similar size (cm range). The excitation is harmonic in each case. The results presented for this work are based on simulations using the same model as described earlier, with minimized hysteresis and negligible eddy current damping. For this work, the acceleration amplitude corresponds to an excitation force amplitude of 50mN acting on a 0.18 kg proof mass. Our frequency value is the resonance frequency of the simulation model under 50mN excitation (see Fig. 13).

Ref	Size ( $\text{cm}^3$ )	Type	Freq. (Hz)	Acceleration amplitude ( $9.82 \text{ m/s}^2$ )	Average Power (mW)	Performance metric ( $\mu\text{W}/\text{cm}^3/\text{g}^2$ )	Relative Bandwidth (%)	$L_z$ (cm)
[35]	8.1	EM	16	1	0.07	8.48	38	1.56 <sup>1</sup>
[36]	19.9	EM/PE	17	0.8	1.8	141.3	26.5	4.8
[37]	53.4	EM/PE	17	0.4	1.98	231.5	58.8	2.05
[38]	397	EM	23	0.51	3.36	32.5	49	2.65
[39]	63	EM	24	1	35	495.5	37.5	7
Ours	19.4	EM	22	0.028	0.03	1712.2	81.8	1.80

1. We calculate a minimum length of 1.85 cm based on the information specified in reference text, in which case the total size and performance metric would need adjustment.

## 4. Conclusion

This work presents a novel EH concept for efficiently harvesting energy from low frequency and low amplitude vibrations. The spring balanced displacements of a small air gap within a magnetic circuit are used to generate large magnetic flux variations for relatively small movements. The EH allows for frequency tuning by adjusting the relative position of the spring. A simulation model is verified to show performance and characteristics comparable to equivalent measurements in the lab. The same results indicate that the principles of the proposed concept still hold under significant hysteresis. Our simulations also show that the degree of hysteresis can be drastically reduced by suitable material choice and that this enables lower resonance frequencies and larger power output in accordance with the proposed concept. Finally, we show that the performance of our EH, under stochastic vibration conditions, matches the performance under harmonic excitation of equivalent amplitude.

For the low-hysteresis configuration used in this work, the EMEH has a tunable resonance frequency down to approx. 20 Hz, with a sensitivity (shift in frequency per change in spring offset) between  $0.14 \text{ Hz}/\mu\text{m}$  and  $0.7 \text{ Hz}/\mu\text{m}$  in the range  $2.533 \text{ mm} \leq \beta \leq 2.548 \text{ mm}$  (nonlinear sensitivity). The maximum RMS power achieved from a harmonic signal at 22 Hz and acceleration amplitude of  $0.028 \text{ g}$  (corresponding to an average base excitation amplitude of  $14.4 \mu\text{m}$ ) is  $26.5 \mu\text{W}$ . Measured vibration data, with most spectral power around 40 Hz and with a mean acceleration of  $0.039 \text{ g}$ , was also used in simulation and resulted in a mean power of  $52 \mu\text{W}$ .

The simulation results show potential performance metrics comparable to state of the art EH. From a set of comparable EH (Table 6) our simulations indicate we can achieve the highest power metric of  $1712.2 \mu\text{W}/\text{cm}^3/\text{g}^2$  while maintaining the largest relative bandwidth of 81.8%.

This design shows promising results regarding generated output power for safety sensors in modern automotive vehicles. The large normalized power density and relative bandwidth of our EMEH, together with results using in-situ vibration data, show that we can potentially generate a useful power output when harvesting energy in-car during normal road conditions, without making use of any dynamic tuning. Although the full frequency tuning potential is not explored, we show that the tuning range of a single device is at least 20 Hz to 45 Hz, a useful range considering typical in-car vibrations. Considering the simplicity and robustness of our design, our EMEH could become a competitive alternative for use not only for this automotive application but also for other practical situations where only very small excitation signals exist such as in machinery or construction equipment.

## CRediT authorship contribution statement

**Johan Bjurström:** Conceptualization, Methodology, Software, Validation, Visualization, Investigation, Data curation, Writing – original draft, Formal analysis. **Fredrik Ohlsson:** Writing – review & editing, Methodology. **Andreas Vikerfors:** Visualization, Methodology. **Cristina Rusu:** Conceptualization, Methodology, Supervision, Resources, Project administration, Funding acquisition. **Christer Johansson:** Writing – review & editing, Methodology.

## Declaration of Competing Interest

The authors declare that they have no known competing financial interests or personal relationships that could have appeared to influence the work reported in this paper.

## Acknowledgments

This work has received funding from Swedish Foundation for Strategic Research in the program for ‘Research Institute PhD’ (grant no. FID16-0055) and the Sweden’s Innovation Agency, Vinnova, grant Challenge-Driven Innovation ‘Energy Toolkit’ (no. 2017-03725).

## References

- [1] Fahmy HMA. Wireless Sensor Networks. Cham: Springer International Publishing; 2020. <https://doi.org/10.1007/978-3-030-29700-8>.
- [2] Garg N, Garg R. Energy harvesting in IoT devices: A survey. In: 2017 International Conference on Intelligent Sustainable Systems (ICISS), IEEE; 2017. <https://doi.org/10.1109/ISSI.2017.8389371>.
- [3] Zeadally S, Shaikh FK, Talpur A, Sheng QZ. Design architectures for energy harvesting in the Internet of Things. *Renew Sustain Energy Rev* 2020;128:109901.
- [4] Chen P, An J, Shu S, Cheng R, Nie J, Jiang T, et al. Super-durable, low-wear, and high-performance fur-brush triboelectric nanogenerator for wind and water energy harvesting for smart agriculture. *Adv Energy Mater* 2021;11(9):2003066.
- [5] Sharma H, Haque A, Jaffery ZA. Maximization of wireless sensor network lifetime using solar energy harvesting for smart agriculture monitoring. *Ad Hoc Netw* 2019; 94:101966.
- [6] Sadowski S, Spachos P. Wireless technologies for smart agricultural monitoring using internet of things devices with energy harvesting capabilities. *Comput Electron Agric* 2020;172:105338.
- [7] Xu C, Song Y, Han M, Zhang H. Portable and wearable self-powered systems based on emerging energy harvesting technology. *Microsyst Nanoeng* 2021;7. <https://doi.org/10.1038/s41378-021-00248-z>.
- [8] Shi Q, Dong B, He T, Sun Z, Zhu J, Zhang Z, et al. Progress in wearable electronics/ photonics—Moving toward the era of artificial intelligence and internet of things. *InfoMat* 2020;2(6):1131–62.
- [9] Maurya D, Kumar P, Khaleghian S, Sriramdas R, Kang MG, Kishore RA, et al. Energy harvesting and strain sensing in smart tire for next generation autonomous vehicles. *Appl Energy* 2018;232:312–22.
- [10] Mondal S, Wijewardena K, Karapuswami S, Kumar D, Chahal P, Ghannam M, et al. A Wireless Battery-less Seat Sensor for Autonomous Vehicles. 2020 IEEE 70th Electronic Components and Technology Conference (ECTC), IEEE; 2020. <https://doi.org/10.1109/ECTC32862.2020.00357>.
- [11] Rui X, Zeng Z, Zhang Y, Li Y, Feng H, Huang X, et al. Design and experimental investigation of a self-tuning piezoelectric energy harvesting system for intelligent vehicle wheels. *IEEE Trans Veh Technol* 2020;69(2):1440–51.
- [12] Benchemoul M, Ferin G, Rosinski B, Bantignies C, Hoang T, Vince P, et al. Wireless Inertial Sensing Platform Self-Powered by Piezoelectric Energy Harvester for Industrial Predictive Maintenance. 2018 IEEE International Ultrasonics Symposium (IUS), IEEE; 2018. <https://doi.org/10.1109/ULTSYM.2018.8580029>.
- [13] Rubes O, Chalupa J, Ksica F, Hadas Z. Development and experimental validation of self-powered wireless vibration sensor node using vibration energy harvester. *Mech Syst Sig Process* 2021;160:107890.
- [14] Shen Y, Lu K. Scavenging power from ultra-low frequency and large amplitude vibration source through a new non-resonant electromagnetic energy harvester. *Energy Convers Manage* 2020;222:113233.
- [15] Fu H, Theodossiadis S, Gunn B, Abdallah I, Chatzi E. Ultra-low frequency energy harvesting using bi-stability and rotary-translational motion in a magnet-tethered oscillator. *Nonlinear Dyn* 2020;101(4):2131–43.
- [16] Wang L, Chen R, Ren L, Xia H, Zhang Y. Design and experimental study of a bistable magnetoelectric vibration energy harvester with nonlinear magnetic force scavenging structure. *Int J Appl Electromagnet Mech* 2019;60(4):489–502.
- [17] Halim MA, Kim DH, Park JY. Low frequency vibration energy harvester using stopper-engaged dynamic magnifier for increased power and wide bandwidth. *J Electric Eng Technol* 2016;11(3):707–14.
- [18] Li K, He X, Wang X, Jiang S. A Nonlinear electromagnetic energy harvesting system for self-powered wireless sensor nodes. *J Sens Actuator Netw* 2019;8(1):18.
- [19] Wang X, Chen C, Wang Na, San H, Yu Y, Halvorsen E, et al. A frequency and bandwidth tunable piezoelectric vibration energy harvester using multiple nonlinear techniques. *Appl Energy* 2017;190:368–75.
- [20] Tri Nguyen H, Genov DA, Bardaweel H. Vibration energy harvesting using magnetic spring based nonlinear oscillators: design strategies and insights. *Appl Energy* 2020;269:115102.
- [21] Ghandchi Tehrani M, Elliott SJ. Extending the dynamic range of an energy harvester using nonlinear damping. *J Sound Vib* 2014;333(3):623–9.
- [22] Triplett A, Quinn DD. The effect of non-linear piezoelectric coupling on vibration-based energy harvesting. *J Intell Mater Syst Struct* 2009;20(16):1959–67.
- [23] Cao S, Sun S, Zheng J, Wang B, Wan L, Pan R, et al. Modeling and analysis of Galenol cantilever vibration energy harvester with nonlinear magnetic force. *AIP Adv* 2018;8(5):056718.
- [24] Sato T, Igarashi H. A chaotic vibration energy harvester using magnetic material. *Smart Mater Struct* 2015;24(2):025033.
- [25] Jiles DC, Atherton DL. Theory of ferromagnetic hysteresis (invited). *J Appl Phys* 1984;55(6):2115–20.
- [26] Jiles DC, Atherton DL. Theory of ferromagnetic hysteresis. *J Magn Magn Mater* 1986;61:48–60. [https://doi.org/10.1016/0304-8853\(86\)90066-1](https://doi.org/10.1016/0304-8853(86)90066-1).
- [27] Neri I, Travasso F, Mincigrucci R, Vocca H, Orfei F, Gammaitoni L. A real vibration database for kinetic energy harvesting application. *J Intell Mater Syst Struct* 2012; 23:2095–101. <https://doi.org/10.1177/1045389X12444488>.
- [28] Rumiche F, Indacochea JE, Wang ML. Assessment of the effect of microstructure on the magnetic behavior of structural carbon steels using an electromagnetic sensor. *J Mater Eng Perform* 2008;17(4):586–93.
- [29] Ida N, Bastos JPA. In: Electromagnetics and Calculation of Fields. New York, NY: Springer New York; 1997. p. 175–211.
- [30] Wang X, Thomas DWP, Sumner M, Paul J, Cabral SHL. Numerical determination of Jiles-Atherton model parameters. *COMPEL - The International Journal for Computation and Mathematics in Electrical and Electronic Engineering* 2009;28. <https://doi.org/10.1108/03321640910929344>.
- [31] Blad TWA, Tolou N. On the efficiency of energy harvesters: a classification of dynamics in miniaturized generators under low-frequency excitation. *J Intell Mater Syst Struct* 2019;30(16):2436–46.
- [32] Beeby SP, Toral RN, Tudor MJ, Glynn-Jones P, O'Donnell T, Saha CR, et al. A micro electromagnetic generator for vibration energy harvesting. *J Micromech Microeng* 2007;17(7):1257–65.
- [33] Wang M, Yin P, Li Z, Sun Yi, Ding J, Luo J, et al. Harnessing energy from spring suspension systems with a compressive-mode high-power-density piezoelectric transducer. *Energy Convers Manage* 2020;220:113050.
- [34] Moss SD, Payne OR, Hart GA, Ung C. Scaling and power density metrics of electromagnetic vibration energy harvesting devices. *Smart Mater Struct* 2015;24 (2):023001.
- [35] Li Y, Wang X, Zhang S, Zhou C, Qiao D, Tao K. A pendulum-like low frequency electromagnetic vibration energy harvester based on polymer spring and coils. *Polymers* 2021;13:3380. <https://doi.org/10.3390/polym13193380>.
- [36] Tan Q, Fan K, Guo J, Wen T, Gao L, Zhou S. A cantilever-driven rotor for efficient vibration energy harvesting. *Energy* 2021;235:121326. <https://doi.org/10.1016/j.energy.2021.121326>.
- [37] Toyabur RM, Salaududdin M, Cho H, Park JY. A multimodal hybrid energy harvester based on piezoelectric-electromagnetic mechanisms for low-frequency ambient vibrations. *Energy Convers Manage* 2018;168:454–66. <https://doi.org/10.1016/j.enconman.2018.05.018>.
- [38] Xie Z, Huang B, Wang S, Zhou X, Gong Y, Huang W. A hula-hooping-like nonlinear buckled elastic string electromagnetic energy harvester for omnidirectional broadband excitations. *Smart Mater Struct* 2020;29(7):075026. <https://doi.org/10.1088/1361-665X/ab9147>.
- [39] Li Z, Yan Z, Luo J, Yang Z. Performance comparison of electromagnetic energy harvesters based on magnet arrays of alternating polarity and configuration. *Energy Convers Manage* 2019;179:132–40.